Available online at www.sciencedirect.com
ScienceDirect
Trans. Nonferrous Met. Soc. China 35(2025) 1092−1108
Transactions of Nonferrous Metals Society of China
www.tnmsc.cn

Achieving high-strength and high-damping Mg−Gd−Y−Zn−Zr−Nd alloy by regulating LPSO and β' phases

Cong DANG, Jing-feng WANG, Jin-xing WANG, Di YU, Wen-xuan ZHENG, Chang-bing XU, Zi-hong WANG, Le FENG, Xian-hua CHEN, Fu-sheng PAN

National Engineering Research Center for Magnesium Alloys, College of Materials Science and Engineering, Chongqing University, Chongqing 400044, China

Received 25 May 2023; accepted 5 November 2023

Abstract: Suitable heat treatment processes were adopted to regulate the precipitation of the lamellar LPSO phase and β' phase in Mg−Gd−Y−Zn−Zr−Nd alloy. The effects of lamellar LPSO phase and β' phase on the mechanical properties and damping capacity of the alloy were studied systematically. Experimental results demonstrate that the lamellar LPSO phase is more conducive to dynamic recrystallization processes, leading to a high degree of recrystallization and a weak texture intensity, resulting in a higher plasticity and damping capacity. After aging treatment, the β' precipitates exhibit pronounced aging strengthening and increase the number of mobile interfaces, thus enhancing the strength and damping capacity at the same time. Through regulating lamellar LPSO and aged β' phase, the alloy achieves high strength and high damping capacity: ultimate tensile strength of 498 MPa, yield strength of 371 MPa and damping capacity of 0.02 at strain amplitude of 1×10^{-3}.

Key words: Mg−Gd−Y−Zn−Zr−Nd alloy; strength; damping capacity; β' precipitates; LPSO phase

1 Introduction

Magnesium (Mg) and its alloys are receiving more attentions in transportation, vehicles, and aircraft structures due to the increasing need for high-damping performance and lightweight in these applications [1−3]. However, their low strength and ductility restrict their application range. Consequently, there is a persistent objective to develop high-performance Mg alloys with an excellent combination of damping capacity, strength and ductility [4,5]. The damping capacity is closely related to the movement of dislocations. On the one hand, a high damping capacity necessitates effortless dislocation movement on basal plane [6,7]. On the other hand, a high strength requires that dislocations could be obstructed by defects such as second phases, boundaries, and stacking faults [8,9]. As a result, the paradox of high damping capacity and high strength must be addressed promptly.

Over the past few years, wrought Mg−Zn−rare earth (RE) alloys containing long-period stacking ordered (LPSO) phases have attracted considerable interests due to their exceptional mechanical performance [10−12]. On the one hand, as the LPSO phase possesses the RE and/or Zn-enriched atomic layers with a stable short-range ordered structure, it shows a higher Young's modulus (~67 GPa) than the Mg matrix (~40 GPa) [11]. Meanwhile, its special kink deformation mechanism can coordinate the *C*-axis stress, effectively improving the strength and plasticity of magnesium alloys [12]. On the other hand, researches [13−17] indicated that the presence of

Corresponding author: Jing-feng WANG, Tel: +86-18623418623, E-mail: jingfengwang@163.com
DOI: https://doi.org/10.1016/S1003-6326(24)66736-1

the LPSO phase was beneficial to enhancing the damping capacity of Mg alloys. TANG et al [13] reported that the increase of the content of LPSO phase in the as-cast Mg−Zn−Y−Zr alloy simultaneously improved its mechanical properties and damping capacity. YUAN et al [14] observed that adding more Zn into Mg−7Gd−3Y−1Nd−0.5Zr alloy led to an improvement of mechanical properties and damping capacity, which was ascribed to the formation of bulk 14H-LPSO phase. In Mg−Cu−Mn−Zn−Y [15] and Mg−Zn−Y−Zr [16] alloys, WANG et al also found that the LPSO phase enhanced mechanical properties while retaining high damping capacity.

Aging treatment is known to be a highly effective technique for reinforcing Mg alloys via the formation of high-density and fine precipitates, which produces an evident precipitation strengthening effect [18]. This study primarily delves into the correlation among LPSO phase, precipitated phases, mechanical properties and damping capacity in Mg alloys. Earlier researches have reported that incoherent second-phase particles characterized by uniform density and distribution can improve room-temperature damping capacity by fostering more mobile dislocations at phase boundaries during damping test [19,20]. The LPSO phase and aging phase can enhance the mechanical properties of Mg alloys, while the combined effect of both on the damping response of alloys hasn't been positively established.

In this work, a regulation in microstructure for preparing a high-strength and high-damping capacity Mg−Gd−Y−Zn−Zr−Nd alloy was proposed. The method involved controlling the post-extrusion alloy structure through pre-extrusion heat treatment and aging treatment process. The effect of the lamellar LPSO phase on the dynamic recrystallization behavior, mechanical properties and damping capacity of the Mg alloy was investigated. Additionally, the influence of the aging phase on both the mechanical properties and damping capacity of the alloy was studied.

2 Experimental

The Mg−10Gd−2Y−1Zn−0.5Zr−0.2Nd (wt.%) alloys were utilized in this study. The specimens with 80 mm in diameter and 50 mm in length were cut from a semi-continuous casting alloy. These samples were subjected to a solid solution process at 540 °C for 4 h, followed by isothermal aging at 400 °C for 20 min. Subsequently, the as-cast alloy and heat-treated alloy were extruded at 400 °C, yielding rod-shaped bars with a diameter of 25 mm and an extrusion ratio of 11:1. The resulting as-extruded samples were designated as H1 and H2, respectively. These as-extruded samples were aged at 200 °C for 48 h, named as AH1 and AH2, respectively.

The as-cast and extruded alloy samples were ground and then etched by 5% nitric acid alcohol solution. The microstructure of the specimens was analyzed through various microscopic techniques, such as Olympus optical microscope (OM), scanning electron microscope (SEM, EOL JSM−7800F) operating at 15 kV and 10 mA, and the transmission electron microscope (TEM, Zeiss Libra 200 FE-TEM) operating at an accelerating voltage of 200 kV. The corresponding energy spectrum analysis was conducted using an energy dispersive X-ray spectrometer (EDS) accompanied with SEM and TEM. Additionally, the electron backscattered diffraction (EBSD) analysis was operated for H1 and H2 alloys at 15 kV, 10 mA with 70° tilt and scanning step sizes of 0.28 and 0.7 μm, respectively. The EBSD data were then analyzed by HKL-Channel 5.

Tensile samples with a gauge length of 30 mm and a diameter of 5 mm were prepared from the as-extruded alloys, and their tensile properties were evaluated on a Shimadzu CMT-5105 material testing machine at a room temperature with an initial strain rate of 0.001 s^{-1}. The tension tests were repeated three times for each as-extruded alloy.

To evaluate the damping capacity, a single-cantilever vibration mode dynamic mechanical analyzer (DMA) (Q800 from TA Instruments) was used. Damping capacity was evaluated by $Q^{-1}=\tan\varphi$, where φ is the lag angle between the applied strain and response stress. The test samples with the size of 45 mm × 5 mm × 2 mm were prepared using electrical discharge machining. The tests gauging the dependence of damping capacity on strain were carried out over a strain amplitude (ε) ranging from 1×10^{-5} to 2×10^{-3} at a room temperature with the vibration frequency (f) of 1 Hz. The damping tests were repeated two times for each as-extruded alloy.

3 Results

3.1 Microstructure prior to extrusion

Figure 1 shows the XRD patterns of alloys with and without heat treatment. The as-cast alloy consists of the LPSO phase, Mg_5RE-type and Mg_3RE-type phases. After heat treatment, the alloy consists primarily of the LPSO and Mg_5RE-type phases with the absence of the Mg_3RE-type phase. Figure 2 displays their corresponding microstructure. The fishbone-like Mg_3RE-type phase (marked by blue arrows) fully vanishes after heat treatment. Figures 2(b, d) show SEM-BSE images. The bright fine particles are identified as Mg_5RE-type phases primarily distributed along grain boundaries and slightly in grain interior. The LPSO phase contains a lower proportion of rare earth elements than Mg_5RE-type, thus appearing bright gray in color. The bulk LPSO phase in the as-cast H1 alloy is predominantly distributed at grain boundaries. Based on the TEM image analysis (Figs. 2(e, f)), the lamellar structure is 14H-LPSO phase (marked by red arrows). The lamellar LPSO phases are mainly distributed in grain interior. In addition, there are Zr-rich secondary particles appearing in Mg matrix.

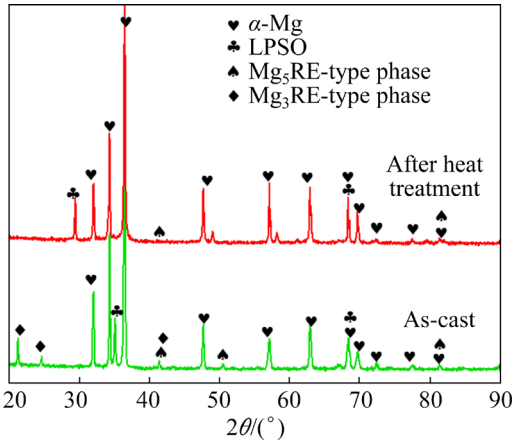

Fig. 1 XRD patterns of cast alloys with and without heat treatment

3.2 Microstructure after extrusion

Figure 3 illustrates the microstructure of the as-extruded alloys. For the H2 alloy with heat treatment, bulk LPSO phases and Mg_5RE-type phases are distributed along grain boundaries, and the large un-recrystallized (unDRXed) grains are surrounded by fine dynamic recrystallized (DRXed) grains (in Figs. 4(d−f)). In the large unDRXed grains, the lamellar LPSO phases and kink bands are observed. Interestingly, the lengthwise direction of the lamellar LPSO phase is identical with the

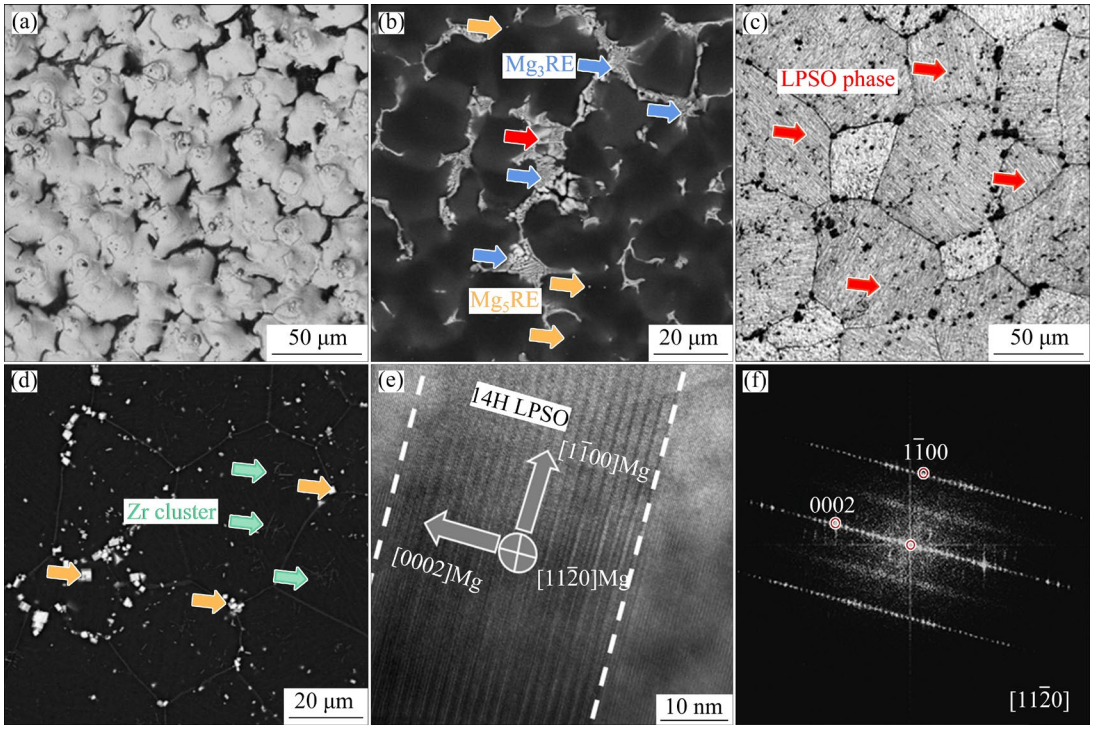

Fig. 2 Microstructure of cast alloys: (a, b) Without heat treatment; (c, d) With heat treatment; (e) High resolution TEM image of lamellar LPSO phase; (f) Corresponding diffraction pattern

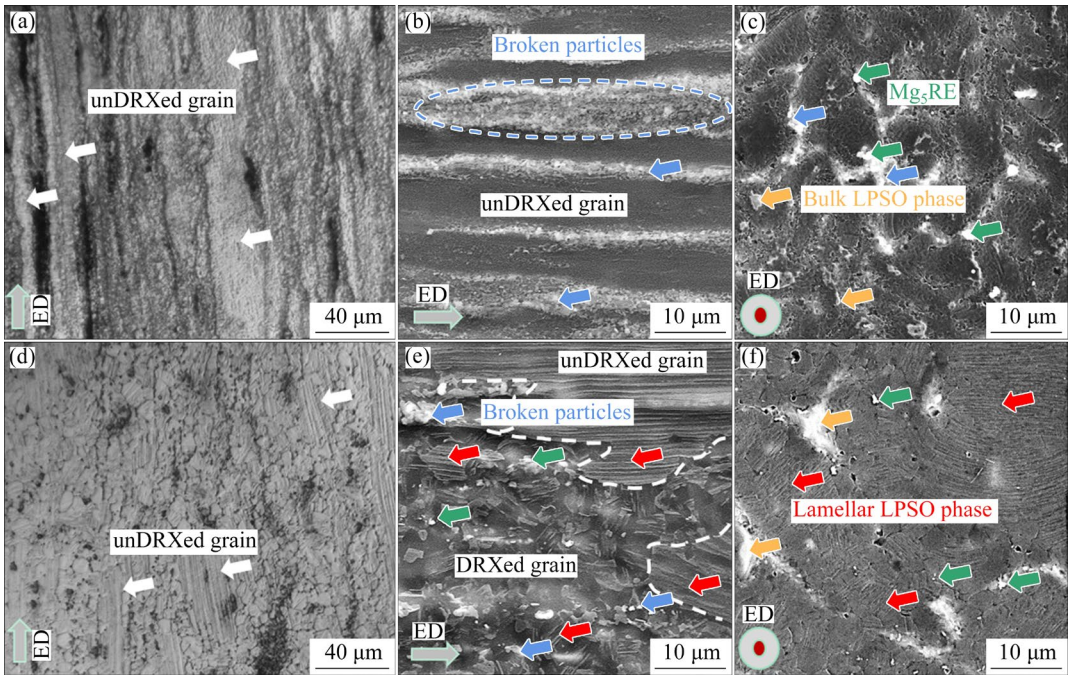

Fig. 3 Microstructure of alloys after extrusion: (a−c) H1 alloy without heat treatment; (d−f) H2 alloy with heat treatment

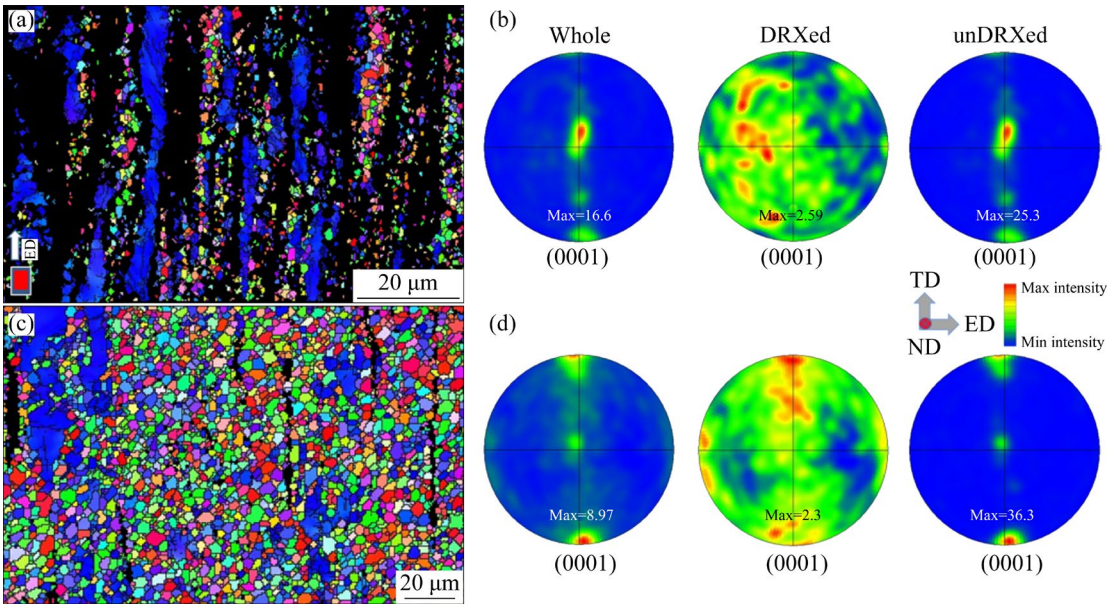

Fig. 4 Analysis result of EBSD: (a, c) Inverse pole figure; (b, d) Pole figure; (a, b) H1 alloy without heat treatment; (c, d) H2 alloy with heat treatment

extruded direction, which has been observed in some other studies as well [18]. However, in the DRXed grains, not all DRXed grains have lamellar LPSO phases. For the H1 alloy without heat treatment, there are a large volume fraction of unDRXed grains. Fine secondary phases (bulk LPSO phase, Mg_5RE-type and Mg_3RE-type phases) present a streamline distribution along the grain boundaries. The fine Mg_3RE-type phases indicate that the massive Mg_3RE-type phases are broken after extrusion. No visible lamellar LPSO phases can be found in Figs. 3(a−c). The unDRXed grain is observed in both alloys after extrusion, and the area of unDRXed grain in the H1 alloy is larger than in the H2 alloy, which implies that the presence of lamellar LPSO phase is beneficial to the dynamic

recrystallization process, while numerous broken particles hinder the dynamic recrystallization process.

Figure 4 displays the inverse pole figure (IPF) and pole figure of the H1 and H2 alloys. The H1 alloy contains a higher area of unDRXed grains compared with the H2 alloy, and the DRXed grain size of the H1 alloy is smaller than that of the H2 alloy. It is obvious that the DRXed grains show a random texture with low intensity in these two alloys (as shown in Figs. 4(b, d)). However, the large volume fraction of unDRXed grain in the H1 alloy results in a strong basal texture with a value of 16.6. The H2 alloy has a high volume fraction of DRXed grain and displays a relatively weak basal fiber texture with a value of 8.97.

3.3 Microstructure after aging treatment

Significant lamellar LPSO phases are observed in both DRXed and unDRXed grains of the AH2 alloy (Figs. 5(a, c)). Fine secondary phases are distributed along grain boundaries, which are considered as Mg_5RE-type phases precipitated from the supersaturated Mg matrix during the extrusion, according to the corresponding diffraction pattern (Fig. 5(e)) [21]. In addition to the lamellar LPSO phases, a fine lamellar structure is detected (marked by the yellow dotted line) in DRXed grain. The fine lamellar structure under higher magnification (Fig. 5(b)) exhibits an obvious contrast difference compared with the Mg matrix. According to the analysis of HAADF-STEM images and the corresponding diffraction pattern (Fig. 5(d)), the fine lamellar structure is identified as stacking faults (SFs). Segregated atoms, such as Gd, Y, Nd and Zn, contribute to the bright contrast of these SFs. Among the solute-segregated SFs, there are several small distorted regions (marked by orange arrows). According to the corresponding diffraction pattern, these distorted regions are identified as the nano-β' phases. It can be concluded that a significant amount of nano-β' aging phases precipitate during the aging process, and the solute-segregated SFs restrict its growth. In Fig. 5(c), a DRXed grain without lamellar LPSO phases or SFs (marked by the green dotted line) is observed, indicating that the lamellar LPSO phase dissolves in Mg matrix during the extrusion process.

For the AH1 alloy, there are a large number of secondary phases in the Mg matrix (as shown in Fig. 6(a)). In the fine DRXed grains, a few lamellar LPSO phases or solute-segregated SFs are present,

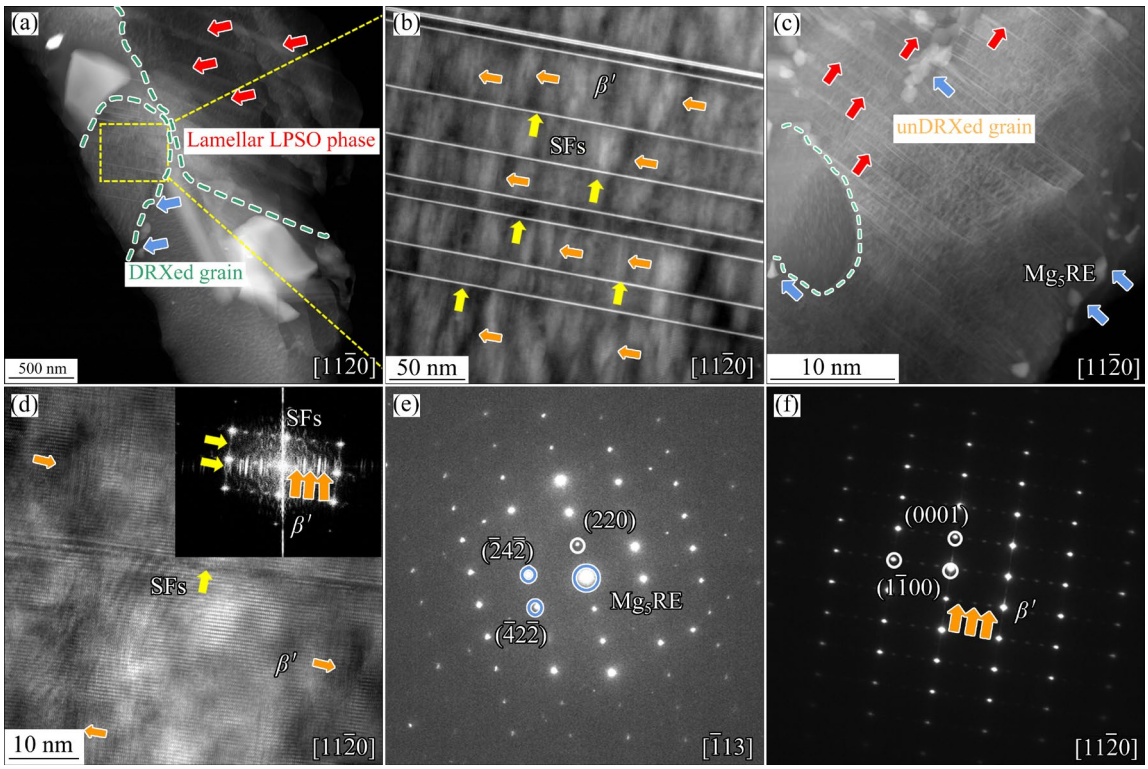

Fig. 5 TEM images of H2 alloy with solution treatment after aging process (a−c); corresponding high resolution TEM image (d); selected area electron diffraction patterns of Mg_5RE (e) and β' precipitate (f)

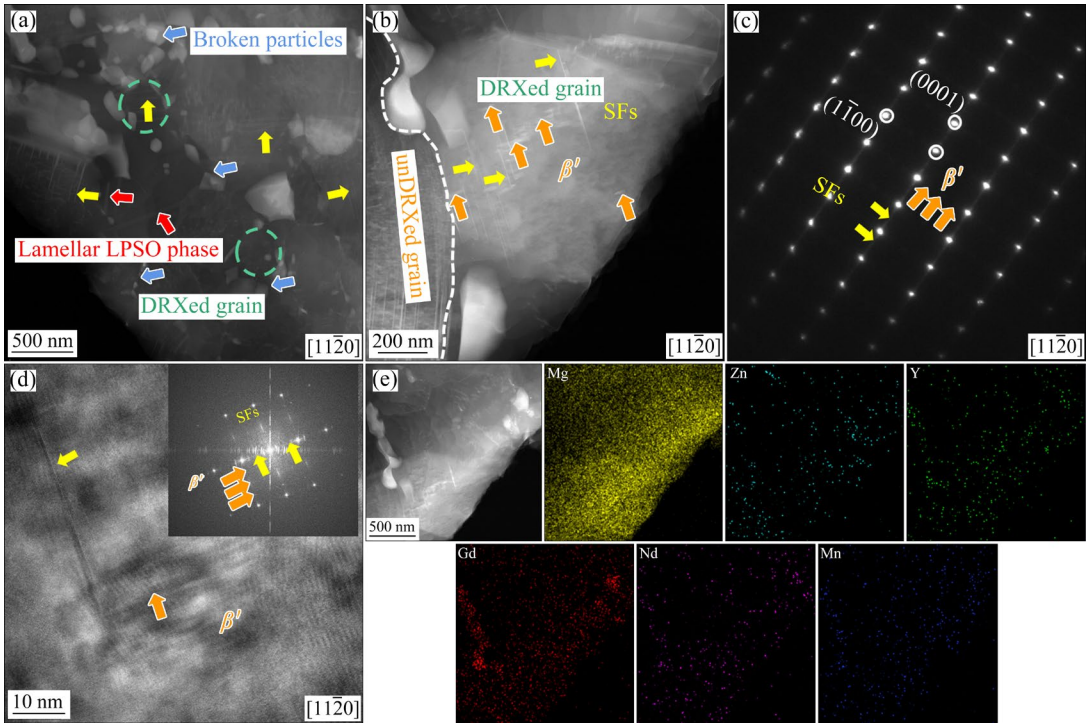

Fig. 6 TEM images of H1 alloy without solution treatment after ageing process (a, b); selected area electron diffraction patterns of β' precipitates (c); high resolution TEM image (d); EDS mappings (e)

while dense solute-segregated SFs are observed in the large unDRXed grains (as shown in Fig. 6(b)). According to the selected area diffraction pattern (Fig. 6(c)), a vague diffraction pattern of β' aging phases is observed. A relatively clear diffraction pattern of β' aging phases emerges, and the SFs are visible in the HAADF-STEM images and corresponding diffraction pattern in Fig. 6(d). Due to a small amount of solute atoms in the H1 alloy, only a few nano-β' phases precipitate during aging process. Based on the EDS-mappings (Fig. 6(e)), these secondary phases are RE-rich phases distributed along the grain boundaries. Combined with the XRD and SEM results, these secondary phases consist of Mg_5RE-type and Mg_3RE-type phases. Thus, the massive Mg_3RE-type phases in the as-cast alloy break into fine secondary particles during the extrusion process.

3.4 Mechanical properties of extruded and aged alloy

Figure 7 displays the engineering stress−strain curve of the as-extruded and aged alloys, while Table 1 presents the corresponding mechanical properties of each alloy. The H1 alloy shows a high ultimate tensile strength (UTS) of 471 MPa and a yield strength (YS) of 386 MPa, but a poor plasticity of only 3.6%. In contrast, the H2 alloy exhibits a relatively low UTS of 406 MPa and YS

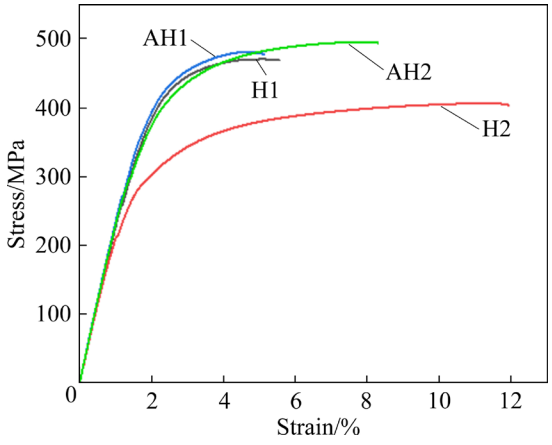

Fig. 7 Engineering stress−strain curve of as-extruded alloys (H1 and H2) and aged alloys (AH1 and AH2)

Table 1 Mechanical properties of different alloys

Alloy	UTS/MPa	YS/MPa	EL/%
H1	471±3	386±5	3.6±0.5
AH1	481±2	404±6	3.1±0.4
H2	406±1.5	271±4	10.1±1.2
AH2	498±3	371±5	6.2±0.8

of 271 MPa, but a good plasticity up to 10.1%. The yield strength of the H1 alloy is 117 MPa higher than that of the extruded H2 alloy. After aging treatment, the strength of H1 alloy is not significantly improved. The AH1 alloy shows UTS of 481 MPa, YS of 404 MPa and EL of 3.1%. However, there are obvious improvement of the strength and the decrease of plasticity in the H2 alloy after aging treatment. The AH2 alloy exhibits UTS of 498 MPa, YS of 371 MPa and EL of 6.2%. Compared with the H2 alloy, the yield strength of AH2 alloy is enhanced by 100 MPa, which indicates that the aging effect is prominent.

3.5 Damping capacity of extruded and aged alloys

Figure 8 illustrates the damping capacity of extruded and aged alloys. Compared with the H1 alloy, the H2 alloy exhibits a higher damping capacity in the entire strain amplitude range. Between the AH1 and AH2 alloys, the AH2 alloy demonstrates a higher damping capacity in the whole strain amplitude range. The curves of H1 and AH1, H2 and AH2 alloys show similar trends. At low strain amplitude, the damping capacity of the extruded alloy surpasses that of the aged alloy. However, at high strain amplitudes, the damping capacity of the H1 and H2 alloys is lower than that of the AH1 and AH2 alloys when strain amplitude exceeds 2×10^{-4} and 3×10^{-4}, respectively. This phenomenon contradicts the trend observed at lower strain amplitudes. Remarkably, when the strain amplitude is 1×10^{-3}, all alloys exhibit high damping capacity above 0.01, which is considered as high damping Mg alloys [13].

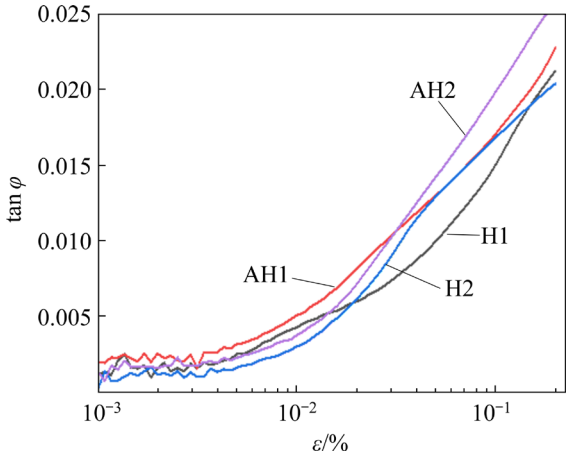

Fig. 8 Damping capacity of different alloys

4 Discussion

4.1 Transformation of LPSO phase

According to the above analysis, there are mainly Mg_3RE-type phases in the as-cast alloy. After solution treatment at 540 °C for 4 h and isothermal aging at 400 °C for 20 min, numerous lamellar LPSO phases are formed in Mg matrix. Therefore, it can be deduced that the transformation of Mg_3RE-type phase into lamellar LPSO phases occurred during the heat treatment. ABE et al [22] suggested that the formation of LPSO phase in Mg−Zn−Y alloy needs three conditions: (1) stacking faults (SFs), (2) adequate solute atoms and (3) solute atoms close to stacking faults. Likewise, the essential conditions required for the formation of the lamellar LPSO phase in this study are satisfied by the presence of stacking faults and sufficient solute atoms.

Figure 9 illustrates the formation process of

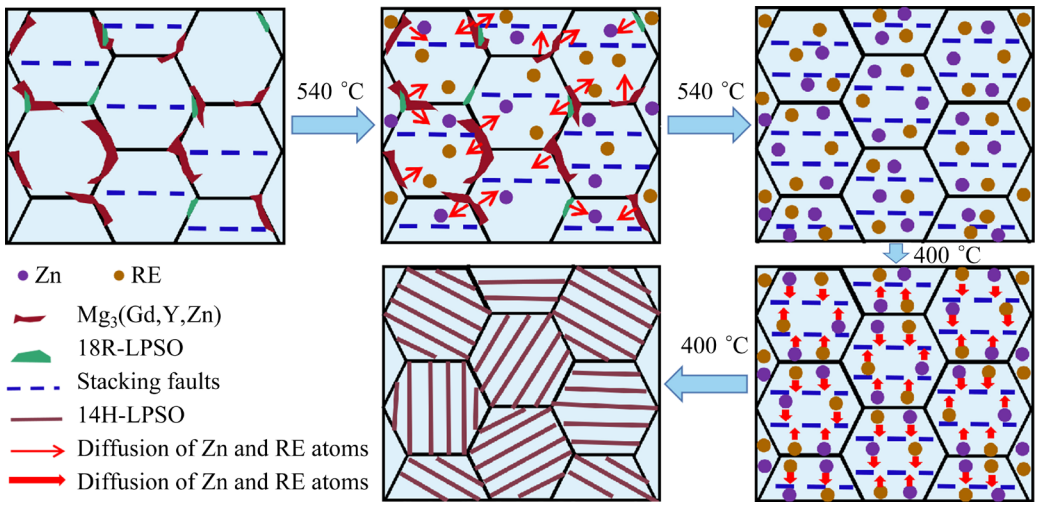

Fig. 9 Schematic of lamellar LPSO phase formation process

the lamellar LPSO phase during heat treatment. Initially, the rare earth (namely Gd, Y, and Nd) atoms and Zn atoms in the Mg_3RE-type phase distributed along grain boundaries dissolve into α-Mg matrix to form a supersaturated solid solution. The abundant solute atoms subsequently lower the stacking fault energy (SFE) of Mg alloys on basal planes, resulting in the formation of numerous stacking faults [23]. Additionally, intrinsic stacking faults are present in α-Mg matrix [24]. During the isothermal aging at 400 °C, the solid solubility of the RE (Gd, Y, Nd) atoms and Zn atoms reduces, which promotes the solute atoms to move towards the stacking faults and ordered arrangement appears. Finally, the lamellar LPSO phases are formed in the grains interior.

4.2 Dynamic recrystallization behavior during extrusion

Following the extrusion at 400 °C, the degree of recrystallization of the H1 alloy without solution treatment is lower than that of the H2 alloy with solution treatment. Broken particles distributed along the grain boundaries in the H1 alloy (in Fig. 3(b)) have potential in hindering grain growth and constraining dynamic recrystallization process. In contrast, the H2 alloy exhibits more and larger DRXed grains, suggesting that the formation of the lamellar LPSO phase is more beneficial to dynamic recrystallization behaviour than Mg_3RE-type phase. The lamellar LPSO phases appear in some DRXed grains, and Mg_5RE-type phases precipitate along the grain boundaries (marked by the green dotted circle in Fig. 5(d)), which implies that the DRX behavior could cause the dissolution and re-precipitation of the lamellar LPSO phase, as well as the precipitation of Mg_5RE phases. Previous studies indicate that the LPSO phase is unstable at high temperatures [25,26]. LPSO phase dissolves completely in the Mg matrix at 540 °C [25], and various LPSO phase morphologies take place after aging process at different temperatures [26]. SU et al [21] further pointed out that the deformation can induce the dissolution of lamellar LPSO phase in Mg−Gd−Zn−Mn alloy during extrusion. In this work, the massive deformation and heat generated by the extrusion process also lead to the dissolution of LPSO phase in the Mg matrix. To understand the effect of lamellar LPSO phase on the DRX behavior, a local area near the unDRXed grain in H2 alloy was investigated using EBSD, as shown in Fig. 10.

The DRXed grains distributed in the unDRXed grain interior and adjacent to secondary phase particles are selected (as shown in Fig. 10(a)). Within the unDRXed grain, numerous lamellar LPSO phases form kink bands with a lengthwise direction consistent with the extruded direction. Based on the KAM maps (as seen in Fig. 10(b)), most of the areas within the unDRXed grain are green and red, indicating a significant distortion. However, the majority of areas in the DRXed grains are blue, representing no distortion. The LPSO phase has an ability to coordinate stress in the *C*-axis direction by twisting itself. Consequently, the angle of the kink boundaries increases with an increase in the degree of deformation [27], resulting in a high local distortion. As a result, these regions with high strain (marked by orange arrows) become nucleation points, as illustrated in Fig. 10(a).

Figures 10(d, g) show the DRXed grains in the unDRXed grain interior and along secondary phase particles, respectively. The orientation distribution of the DRXed grains in unDRXed grain is close to the parent grain, revealing a clear characteristic of continuous dynamic recrystallization process (CDRX), as evidenced in Fig. 10(e). The CDRX is considered as a process that sub-boundaries continuously absorb dislocations, leading to the increase of misorientation angle, the rotation of sub-grains, and the gradual transformation of low angle boundaries (LABs) into high-angle boundaries (HABs). As a result, sub-grains grow into real grains [28]. In Fig. 10(f), the misorientation angle gradually increases with increasing the distance (as depicted by the white arrows A, B and C). The results suggest the existence of dense dislocations and sub-grain boundaries in grain interior, which have the potential to act as nucleation points. Therefore, the mechanism of dynamic recrystallization in grain interior is CDRX.

However, the orientation distribution of the DRXed grains near the secondary particles is more random, indicating that the mechanism of dynamic recrystallization is the discontinuous dynamic recrystallization (DDRX). The DDRX process involves nucleation and growth, which mainly happen on the original grain boundaries through the migration of high-angle boundaries (HABs) [29].

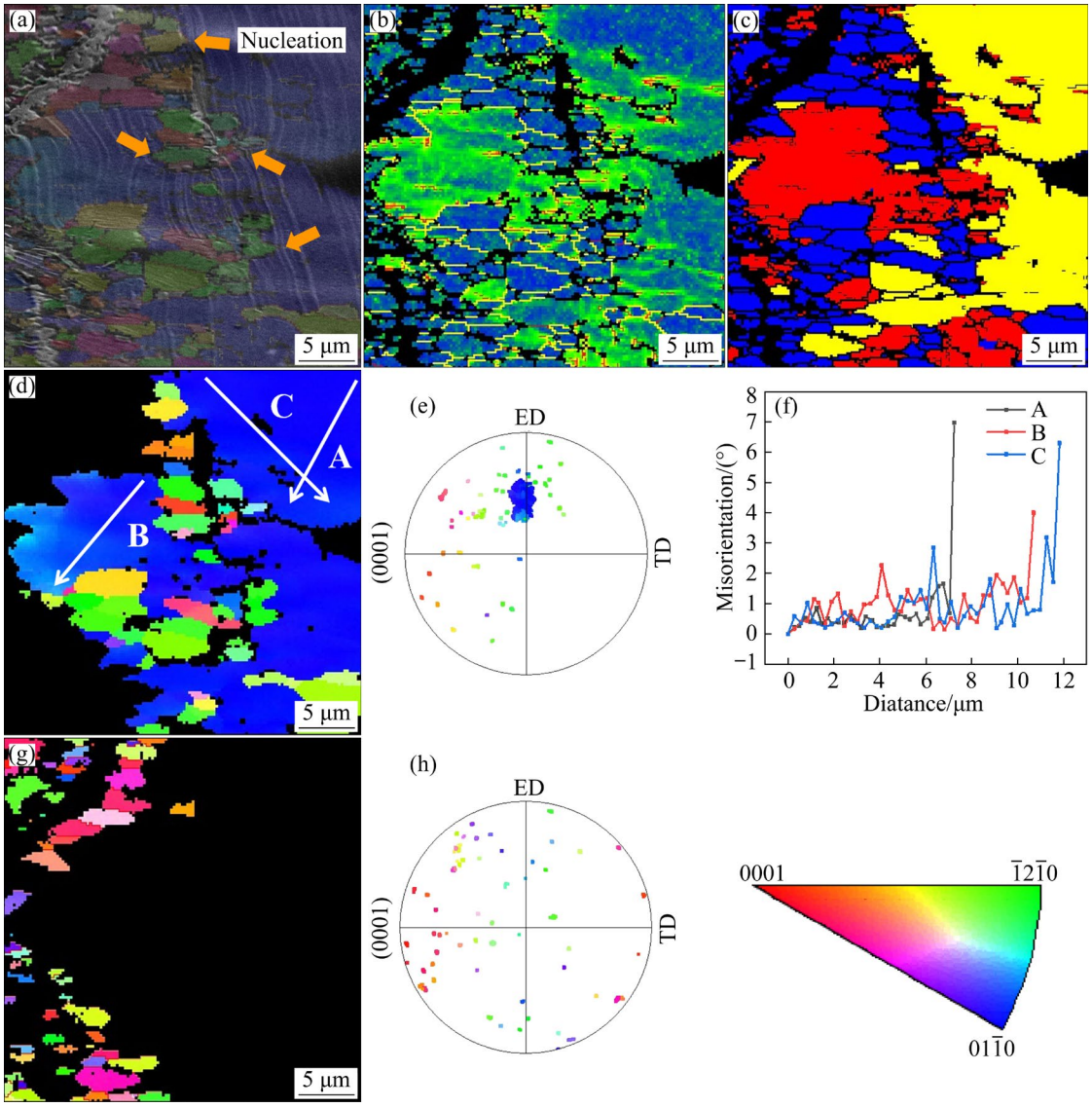

Fig. 10 EBSD analysis of partially extruded alloys: (a) IPF maps; (b) KAM map; (c) Distribution map of recrystallization; (d, e) IPF with unDRXed grain and its internal DRXed grains and corresponding (0001) pole figure; (f) Misorientation calculated by point-to-origin along white arrows (A, B, C) in (d); (g, h) IPF with DRXed grains distributed in secondary phase particles and corresponding (0001) pole figure

Additionally, the presence of the secondary particles can foster dynamic recrystallization (DRX) through the particle-simulated nucleation (PSN) mechanism [30], therefore, the DRXed grains develop preferentially along the secondary particles. The literature [31] showed that the necklace structure in grain boundaries formed by the migration of high-angle boundaries (HABs) mechanism was identified as the DDRX grains, while the finer necklace structure was identified as CDRX grains, whose formation is due to the strain-induced low angle grain boundary (LAGB) mechanism in the kink bands of 14H LPSO phase. Therefore, both DDRX and CDRX mechanisms occur in the H2 alloys during the dynamic recrystallization process.

Based on the above analysis, the dynamic recrystallization process of the H2 alloy containing lamellar LPSO phases during hot extrusion is summarized in Fig. 11. During the initial stage of extrusion, the original grains elongate and result in the accumulation of numerous dislocations at the original grain boundaries. This process triggers the PSN and DDRX mechanisms, leading to the nucleation of new grains located preferentially at the original grain boundaries. However, the presence

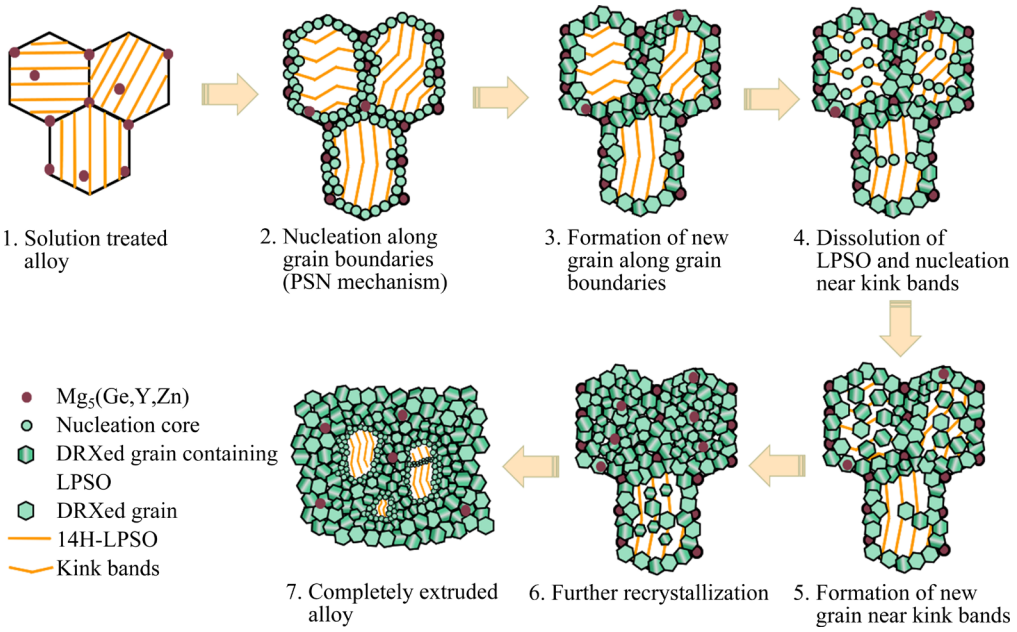

Fig. 11 DRX process in solution treated alloy during hot extrusion

of the lamellar LPSO phase inhibits the movement of the dislocations, causing the accumulation of high-density dislocations at the LPSO phase/α-Mg interface. This continuous increase in strain causes the accumulation of even higher densities of dislocations and the subsequent formation of kink bands [32]. Meanwhile, the new grains nucleate at the kink bands. However, the high-density dislocations serve as efficient channels for the rapid diffusion of the solute atoms at high temperatures [33], promoting the dissolution of local lamellar LPSO phase/SFs. The dissolution of the local lamellar LPSO phases/SFs contributes to the development of a supersaturated solution during the growth of newly-formed grains. The presence of the solute atoms results in a reduction of the stacking fault energy, leading to a re-formation of the lamellar LPSO phases/SFs (Fig. 5(a)) [34]. In addition, Mg_5RE-type phases precipitate at the DRXed grain boundaries owing to the segregation of the solute atoms within the supersaturated solution. Since the lengthwise direction of the lamellar LPSO phase is parallel with the extrusion direction, the degree of the deformation is small and the number of nucleation sites for new grains at kink boundaries is reduced, which consequently delays the DRX process. Thus, the unDRXed grains usually are the grains containing the lamellar LPSO phases whose lengthwise direction is parallel with the extrusion direction, as indicated in Fig. 3(e).

4.3 Strengthening mechanism

In general, bimodal grain microstructures can provide higher strength but lower ductility compared to fully equiaxed grains. Previous researches [35,36] have shown that the fine DRXed grains exhibit a random texture, while the coarse unDRXed grains show a strong basal texture in a typical bimodal microstructure of as-extruded Mg alloys with LPSO phases. The microstructure with a higher volume fraction of fine DRX grains is conducive to improve the ductility, while a higher volume fraction of coarse unDRXed grains leads to a high strength. Therefore, a good balance between the strength and ductility can be achieved by controlling the volume fractions of DRXed and unDRXed grains. Several studies have confirmed that a microstructure with an appropriate volume fraction of the DRXed grains and a certain amount of the unDRXed grains has a positive influence on the mechanical properties of Mg alloys. The H1 alloy contains a higher volume fraction of unDRXed grains with a strong basal texture and smaller DRXed grains, which is conducive to enhance the strength of alloy. However, the H2 alloy contains a higher volume fraction of DRXed grains with lower texture, which in turn improves the ductility of alloy.

In addition to the grain boundary strengthening, the second phase strengthening is also a key factor to control the mechanical properties of metals. The

activation of basal dislocation slip is the primary reason for the low strength of Mg alloys at ambient temperature. In the H1 alloy, the main reinforcing phase is Mg_3RE-type phase. Since Mg_3RE-type phase has a high melting point, about 520 °C [37], the bulk Mg_3RE-type phases do not dissolve, but break into smaller particles during extrusion at 400 °C (in Fig. 6(a)). These phases possess high hardness and can effectively hinder dislocations movement, leading to a high strength. However, the irregular shapes of Mg_3RE-type phases cause stress concentration, which makes the cracks form easily. Therefore, the H1 alloy shows a lower ductility.

The H2 alloy mainly contains LPSO phases, including lamellar and bulk LPSO phases. The studies show that Mg alloys containing LPSO phases typically have relatively high strength, which is attributed to the activation of non-basal slip, the suppression of twinning, kinking band strengthening and short-fiber strengthening [38]. The stacking ordered and chemically ordered structure of the LPSO phase results from the co-segregation of RE and Zn atoms, which creates a semi-coherent or coherent interface between LPSO phase and Mg matrix, as well as higher hardness and Young's modulus. As a hard phase, the LPSO phase can inhibit dislocation motion [39]. Moreover, the LPSO phases can provide short-fiber strengthening, retard the propagation of microcracks and prevent failure in Mg alloys [40]. Due to the semi-coherent or coherent interface between the LPSO phase and Mg matrix, when dislocations reach the LPSO/α-Mg interface, some dislocations can be inhibited and accumulate at this interface, while others enter the LPSO phase [41,42]. The accumulation of dislocation at the LPSO/α-Mg interface can lead to stress concentration. However, dislocations entering the LPSO phase can continue moving, thereby playing a more effective role in coordinating stress. In addition, the LPSO phase can increase the critical resolved shear stress (CRSS) of the basal plane, activating non-basal $\langle c+a \rangle$ slip [43]. Thus, the activation of the non-basal dislocation slip and its coordinating effect improve the ductility of Mg alloys.

After aging treatment, the yield strength of AH1 alloy has an enhancement of 10 MPa; however, the yield strength of AH2 alloy has an enhancement of 100 MPa. Because a few β' phases precipitate in the AH1 alloy, a weak precipitation strengthening is shown. Conversely, the AH2 alloy contains numerous β' precipitates (Fig. 5(b)). The β' precipitates are distributed on the prismatic plane, which can effectively impede basal dislocation movement, and result in a strong strengthening effect. In addition to a large number of β' precipitates, Mg matrix contains solute-segregated SFs and lamellar LPSO phases (Fig. 5) that grow along the basal plane. Due to large aspect ratio, solute-segregated SFs and lamellar LPSO phases can bring about a significant strengthening effect. Coincidentally, the orientation relationship of these two phases is perpendicular to each other. As reported [44], when the spacing of lamellar LPSO phases/SFs is narrow enough, the β' phase can interact with the neighboring lamellar LPSO phases/SFs, and the growth of β' phase along the c-axis can be restricted by the lamellar LPSO phases/SFs acting as an obstacle. Consequently, this closed structure composed of the prismatic β' precipitates, solute-segregated SFs and lamellar LPSO phases can exhibit higher strengthening effects than the sole lamellar LPSO phases [45]. However, due to the easy accumulation of dislocations, this structure leads to stress concentration. The AH2 alloy shows a lower ductility than the H2 alloy.

In summary, the significant difference in strength and plasticity between the H1 and H2 alloys is primarily attributed to differences in microstructure and the type of second phase, specifically, the Mg_3RE-type phases and LPSO phase. However, the AH2 alloy exhibits a higher strength than the AH1 alloy due to the significant aging strengthening.

4.4 Damping mechanism

Dislocation damping is regarded as the primary damping mechanism in Mg alloys at room temperature. The Granato and Lücke (G-L) model [46,47] provides a classical theory to explain dislocation damping. According to the G-L model, dislocation lines are pinned by relatively weak pinning points such as solute atoms or vacancies at low strain amplitudes. Similarly, at high strain amplitudes, stronger pining points, such as dislocation nets, precipitates or intermetallic compounds strongly pin the dislocation lines. The total damping capacity (Q^{-1}) can be described as a

sum of the strain-independent damping Q_0^{-1} and the strain-dependent damping Q_a^{-1}:

$$Q^{-1}=Q_0^{-1}+Q_a^{-1} \quad (1)$$

At low strain amplitudes, dislocation lines are impeded by weak pinning points. They move back and forth between these weak pinning points. The Q_0^{-1} can be expressed as follows [46,47]:

$$Q_0^{-1}=\frac{2\Omega(1-\nu)^2\Lambda L_C^4 B\omega}{\pi G b^2} \quad (2)$$

where Ω represents the orientation factor, ν represents Poisson's ratio, B represents the damping constant of dislocation motion, Λ represents the mobile dislocation density, L_C represents the average distance between weak pinning points, ω represents the angular frequency, G represents the shear modulus, and b represents the magnitude of Burger's vector. According to Eq. (2), the strain-independent damping in the low strain amplitude region is primarily affected by the orientation factor (Ω), mobile dislocation density (Λ), and average distance (L_C) between weak pinning points.

The number of weak pinning points affects the value of L_C. Following solid solution treatment, numerous atoms dissolve in Mg matrix, resulting in a great number of weak pinning points. Therefore, compared with the H1 alloy, the value of L_C in H2 alloy is not benefitial to a high damping capacity. The orientation factor reflects the movability of the basal dislocation. Easier basal dislocation slip results in higher damping capacity. In general, the ease of the basal dislocation slip is evaluated by Schmid factor (SF) [48]. A large SF value on the basal plane means more favorable dislocation slip, which is conducive to consume more energy and demonstrates better damping capacity. The average Schmid factor values along the $(0001)\langle 11\bar{2}0\rangle$ basal slip of H1 alloy and H2 alloy are 0.19 and 0.24, respectively. The average SF of the H2 alloy is lower than that of the H1 alloy, indicating that the H2 alloy has the potential for high damping capacity.

Furthermore, at low strain amplitudes, higher moveable dislocation density leads to higher damping capacity. The residual dislocation density can be evaluated through the local misorientation angle [49], as depicted in Fig. 12. High value of kernel average misorientation (KAM) is represented by the green and red regions, while low KAM value is indicated by blue regions in the KAM maps. The H1 alloy displays a higher KAM value than the H2 alloy. Notably, the green and red regions belong to the unDRXed grain. Consequently, there is a high residual dislocation density in the H1 alloy. Nonetheless, high residual dislocation density can result in dislocation slip tangles, reducing the movability of dislocation and leading to a lower damping capacity. Therefore, the H2 alloy exhibits a better damping capacity.

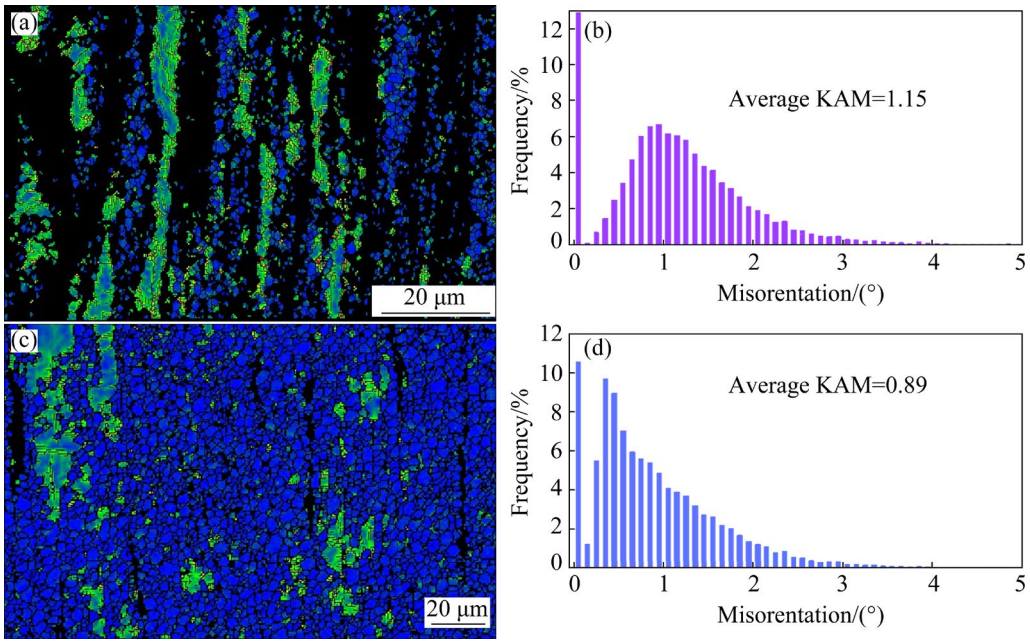

Fig. 12 KAM map (a, c) and distribution (b, d) of H1 (a, b) and H2 (c, d) alloys

Apart from these factors mentioned above, the presence of LPSO phase is also a significant factor. Prior studies [14−16] have demonstrated that Mg alloys with LPSO phase usually exhibit a high damping capacity while retain good mechanical properties. WANG et al [15] has noted that the damping capacity of Mg−Cu−Mn−Zn−Y alloys increased at low strain amplitude with an augmented content of the LPSO phase. To summarize, a higher damping capacity exhibited by the H2 alloy is attributed to its high moveable-dislocation density, high basal Schmid factor and LPSO phase. After aging treatment, the damping capacity of both H1 and H2 alloys decreases at low strain amplitude. As per the G−L model, the decrease in solute atoms correspondingly leads to the longer average distance between weak pinning points, resulting in a higher damping capacity. However, during aging process, precipitates tend to gather at defects such as dislocations, stacking faults, and twin boundaries [21]. Numerous precipitates inhibit dislocation movement, leading to a reduction in damping capacity at low strain amplitude.

At high strain amplitudes, the strain-dependent damping is influenced by the vibration of the dislocation anchored by the strong pinning points. The following expression can be employed to describe this relationship simply [46,47]:

$$Q_{\mathrm{a}}^{-1}=\left(\frac{C_1}{\varepsilon}\right)\exp\left(-\frac{C_2}{\varepsilon}\right) \tag{3}$$

$$C_1=\frac{4\Omega(1-\nu)\Lambda L_{\mathrm{N}}^3}{\pi^2 L_{\mathrm{C}}}C_2 \tag{4}$$

$$C_2=\frac{kb\eta}{L_{\mathrm{C}}} \tag{5}$$

where L_{N} is average distance between strong pinning points. According to Eq. (3), we can deduce a formula: $\ln(\varepsilon\cdot Q_{\mathrm{a}}^{-1})=-C_2/\varepsilon+\ln C_1$ (ε is the strain amplitude). A linear relationship between $\ln(\varepsilon\cdot Q_{\mathrm{a}}^{-1})$ and $1/\varepsilon$ demonstrates that the damping behavior at room temperature is fit for the dislocation damping mechanism. The G-L plots of alloys in different states are shown in Fig. 13. A non-linear relationship between $\ln(\varepsilon\cdot Q_{\mathrm{a}}^{-1})$ and $1/\varepsilon$ exists in all alloys, which means there is not dislocation damping mechanism only. WANG et al [15] attributes this phenomenon to the LPSO phase.

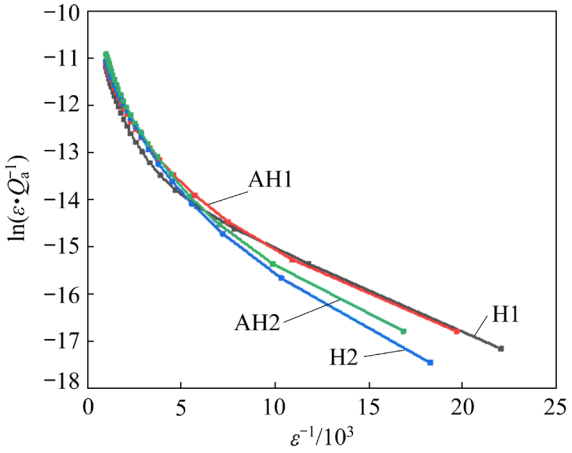

Fig. 13 G-L plots of alloys in different states

In high strain amplitude region, the damping capacity is related to Λ, Ω and L_{N}. Since the Mg matrix contains only a small number of solute atoms, the volume fraction of broken Mg_3RE-type eutectic phases in the H1 alloy is higher than that of the LPSO phase in the H2 alloy, causing the average distance between strong pinning points to be shorter and a lower damping capacity in the H1 alloy. Thus, the damping capacity of the H2 alloy is higher than that of the H1 alloy, which is attributed to higher moveable-dislocation density, higher basal Schmid factor and LPSO phase.

After aging treatment, there is a sudden increase in damping capacity at strain amplitude of approximately 1×10^{-4} in the AH1 and AH2 alloys (Fig. 8). Previous literature has reported that the incoherent second phase particles with a high density and uniform distribution can enhance the room-temperature damping capacity of metal by introducing more mobile dislocations at the phase interface [50]. This implies that the β' precipitate may play a crucial role in the damping properties. Figure 14 displays a high resolution TEM image of β' precipitates along the $[11\bar{2}0]$ direction. It can be seen that the location where the strain occurs is mainly concentrated at the β' phase/α-Mg interface, which means that the β' phase/Mg interfaces are prone to develop dislocations on non-basal planes. As a result, the presence of β' precipitates introduces more movable interfaces in Mg matrix. Figure 15 shows the schematic of microstructure of alloys and dislocation pinning model. When the stress is large enough to drive the movement of β' phase/α-Mg interface, more consumed energy leads to the improvement of damping capacity.

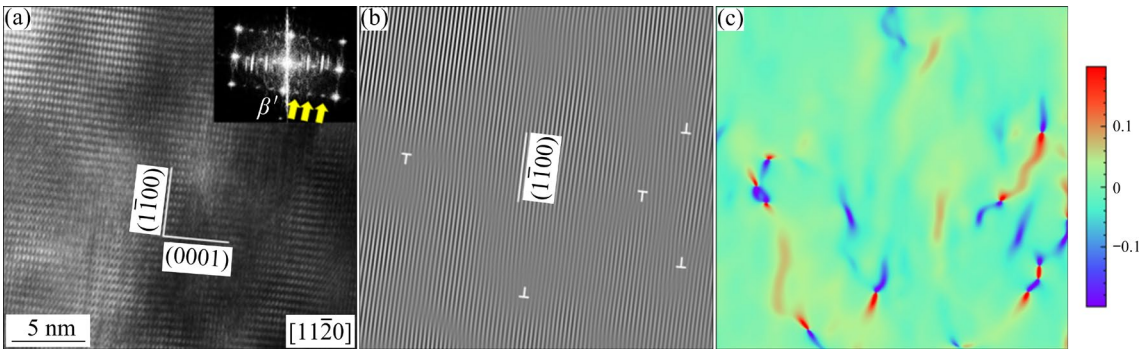

Fig. 14 High resolution TEM image of β' precipitates and Mg matrix along [11$\bar{2}$0] direction: (a) High resolution TEM image of β' precipitates and selected area electron diffraction patterns; (b) Inverse FFT image obtained from {01$\bar{1}$0} reflection, in which dislocation cores are marked by white symbol "⊥"; (c) GPA strain distribution of {1$\bar{1}$00} planes

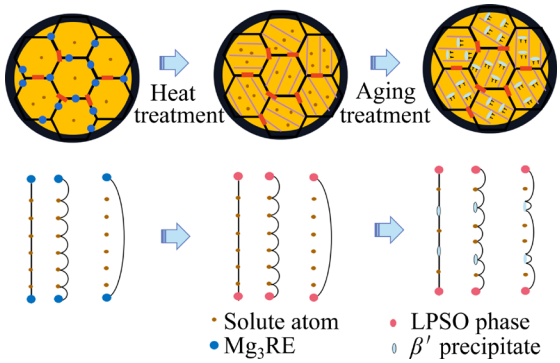

Fig. 15 Schematic of microstructure of alloys and dislocation pinning model

Figure 16 summarizes the Q^{-1} and $\sigma_{0.2}$ of the studied high-strength and high-damping Mg alloys exceeding 200 MPa at room temperature. Generally speaking, the damping capacity and the yield strength are contradicted. WANG et al [43] introduced a large number of defects, such as twins, lamination and dislocation, in the matrix by extrusion and rolling process, achieving the improvement of the damping capacity and strength of the Mg alloy. XU et al [51] improved the damping capacity and yield strength of the Mg alloy by forming a large number of stacking faults in Mg matrix. In this study, the precipitation of lamellar LPSO and aging phases is controlled through solution treatment and aging process, and the balance between the mechanical properties and damping capacity is thus achieved. Although the damping capacity is lower than the above special two alloys, it still possesses a high damping performance and its yield strength is about 1.5 times that of them. Compared with other high-strength and high-damping magnesium alloys [15,16,43,52−54], the prepared alloys show higher strength and damping capacity. Therefore, a novel approach through the pre-extrusion heat treatment and the incorporating aging treatment process for preparing a high-strength and high-damping Mg alloy is presented, which will provide a reference for high-strength and high-damping alloys.

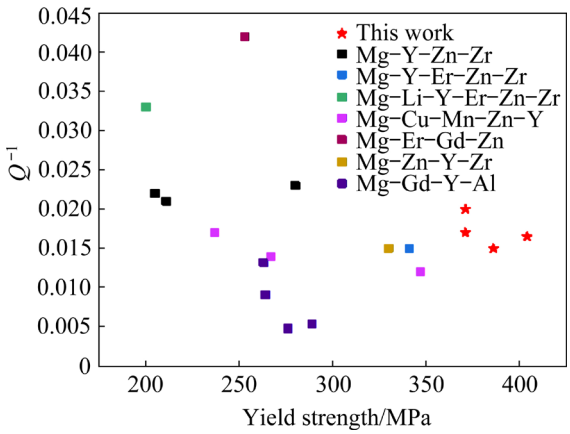

Fig. 16 Yield strength and damping capacity of alloys in comparison with several high-strength and damping alloys [15,16,43,52−54] at room temperature (The strain amplitude is 1×10^{-3} and the forced frequency is 1 Hz)

5 Conclusions

(1) The solution treatment conducted at 540 °C for 4 h and 400 °C for 20 min can effectively eliminate the Mg_3RE-type phases, and facilitate the formation of the lamellar 14H-LPSO phase.

(2) The lamellar LPSO phase has a positive effect on the dynamic recrystallization process. The DRXed grains are preferentially formed along grain

boundaries via the particle-simulated nucleation (PSN) mechanism. Next, the DRXed grains nucleate and grow at the kinking interface of lamellar LPSO phase via the strain-induced low-angle grain boundary (LAGB) mechanism.

(3) The precipitation of a significant number of aged β' phases has two main effects: enhancing the strength of the alloy by aging strengthening, and improving the damping performance through increasing the number of mobile interfaces.

(4) A high-strength and high-damping Mg−Gd−Y−Zn−Zr−Nd alloy is developed by regulating lamellar LPSO and aging β' phase. The ultimate tensile strength is 498 MPa, yield strength is 371 MPa and damping capacity is 0.02 at strain amplitude of 1×10^{-3}.

CRediT authorship contribution statement

Cong DANG: Writing − Original draft; **Jing-feng WANG:** Writing − Review & editing, Funding acquisition; **Jin-xing WANG:** Supervision; **Di YU:** Investigation; **Wen-xuan ZHENG:** Investigation; **Chang-bing XU:** Investigation; **Zi-hong WANG:** Supervision, Writing − Review & editing; **Le FENG:** Data curation, Formal analysis, Supervision; **Xian-hua CHEN:** Methodology, Supervision; **Fu-sheng PAN:** Supervision, Conceptualization.

Declaration of competing interest

The authors declare that they have no known competing financial interests or personal relationships that could have appeared to influence the work reported in this paper.

Acknowledgments

This work is financially supported by the National Key Research and Development Program of China (No. 2021YFB3701100), the National Natural Science Foundation of China (Nos. U20A20234, 51874062), the Postdoctoral Science Foundation of China (Nos. 2023M730390, 2022M710563), and the Natural Science Foundation Commission, China (Nos. CSTB2023NSCQ-BHX0164, CSTB2022NSCQ-BHX0029).

References

[1] HUANG Wen-sen, CHEN Ji-hua, YAN Hong-ge, LI Qiang, XIA Wei-jun, SU Bin, ZHU Wei-jun. Solid solution strengthening and damping capacity of Mg−Ga binary alloys [J]. Transactions of Nonferrous Metals Society of China, 2022, 32: 2852−2865.

[2] DING Zhi-bing, ZHAO Yu-hong, LU Ruo-peng, YUAN Mei-ni, WANG Zhi-jun, LI Hui-jun, HOU Hua. Effect of Zn addition on microstructure and mechanical properties of cast Mg−Gd−Y−Zr alloys [J]. Transactions of Nonferrous Metals Society of China, 2019, 29: 722−734.

[3] DANG Cong, DOU Xiao-xu, WANG Jing-feng, YU Di, WANG Jin-xing, LU Ruo-peng, HOU Hua, ZHAO Yu-hong. Investigations on microstructure and mechanical properties of cast Mg−Gd−Y−Zn−Zr−Nd alloy [J]. Journal of Materials Research and Technology, 2023, 24: 4852−4862.

[4] LI Qian-kun, YAN Hong, CHEN Rong-shi. Effect of rolling reduction on deformation mechanism and twinning behavior of WE43 magnesium alloy [J]. Transactions of Nonferrous Metals Society of China, 2022, 32: 3901−3913.

[5] ZHANG Ke-long, LI Hui-zhong, LIANG Xiao-peng, CHEN Zhi, ZHAO Zi-xuan, TAO Hui, ZHOU Xiong-wen. Effect of aging time on discontinuous precipitates, continuous precipitates and mechanical properties of AZ80A magnesium alloy [J]. Transactions of Nonferrous Metals Society of China, 2022, 32: 2838−2851.

[6] DANG Cong, WANG Jing-feng, WANG Jin-xing, YU Di, ZHENG Wen-xuan, XU Chang-bing, WANG Zi-hong, FENG Le, CHEN Xian-hua, PAN Fu-sheng. An ultrahigh strain-independent damping capacity in Mg−1Mn alloy by cold rolling process [J]. Journal of Materials Research and Technology, 2023; 25: 4330−4341.

[7] DANG Cong, WANG Jing-feng, WANG Jin-xing, YU Di, ZHENG Wen-xuan, XU Chang-bing, WANG Zi-hong, FENG Le, CHEN Xian-hua, PAN Fu-sheng. Simultaneous improvement of strength and damping capacity of Mg−Mn alloy by tailoring bimodal grain structure [J]. Vacuum, 2023, 215: 112275.

[8] LIU Huan, HUANG He, WANG Ce, SUN Jia-peng, BAI Jing, XUE Feng, MA Ai-bin, CHEN Xiao-bo. Recent advances in LPSO-containing wrought magnesium alloys: Relationships between processing, microstructure, and mechanical properties [J]. The Minerals, Metals & Materials Society, 2019, 71: 3314−3327.

[9] LIU Huan, HUANG He, SUN Jia-peng, WANG Ce, BAI Jing, MA Ai-bin, CHEN Xian-hua. Microstructure and mechanical properties of Mg−RE−TM cast alloys containing long period stacking ordered phases: A review [J]. Acta Metallurgica Sinica (English Letters), 2019, 32: 269−285.

[10] HUANG Song, WANG Jing-feng, HOU Fan, HUANG Xiu-hong, PAN Fu-sheng. Effect of Gd and Y contents on the microstructural evolution of long period stacking ordered phase and the corresponding mechanical properties in Mg−Gd−Y−Zn−Mn alloys [J]. Materials Science and Engineering A, 2014, 612: 363−370.

[11] HAGIHARA K, OKAMOTO T, IZUNO H, YAMASAKI M, MATSUSHITA M, NAKANO T, KAWAMURA Y. Plastic deformation behavior of 10H-type synchronized LPSO phase in a Mg−Zn−Y system [J]. Acta Materialia, 2016, 109: 90−102.

[12] WANG Kui, WANG Jing-feng, HUANG Song, DOU Xiao-xu, WANG Jin-xing, WANG Cun-long. Formation of an abnormal texture in Mg−Gd−Y−Zn−Mn alloy and its effect on mechanical properties by altering extrusion parameters [J]. Materials Science and Engineering A, 2022, 831: 142270.

[13] TANG Yan-xia, LI Bo, TANG Hong-xia, XU Yong-chun, GAO Ya-ping, WANG Li-hua, GUAN Jin-yu. Effect of long period stacking ordered structure on mechanical and damping properties of as-cast Mg−Zn−Y−Zr alloy [J]. Materials Science and Engineering A, 2015, 640: 287−294.

[14] YUAN Jia-wei, LI Ting, ZHANG Kui, LI Meng, LI Xing-gang, LI Yong-jun, MA Ming-long, SHI Guo-liang. Effect of Zn content on the microstructures, mechanical properties, and damping capacities of Mg−7Gd−3Y−1Nd−0.5Zr based alloys [J]. Journal of Alloys and Compounds, 2019, 773: 919−926.

[15] WANG Jing-feng, WEI Wen-wen, HUANG Xue-fei, LI Long, PAN Fu-sheng. Preparation and properties of Mg−Cu−Mn−Zn−Y damping magnesium alloy [J]. Materials Science and Engineering A, 2011, 528: 6484−6488.

[16] WANG Jing-feng, SONG Peng-fei, GAO Shan, HUANG Xue-feng, SHI Zhang-zhi, Pan Fu-sheng. Effects of Zn on the microstructure, mechanical properties, and damping capacity of Mg−Zn−Y−Zr alloys [J]. Materials Science and Engineering A, 2011, 528: 5914−5920.

[17] DANG Cong, WANG Jing-feng, WANG Jin-xing, YU Di, ZHENG Wen-xuan, XU Chang-bing, LU Ruo-peng. Effect of lamellar LPSO phase on mechanical properties and damping capacity in cast magnesium alloys [J]. Journal of Materials Research and Technology, 2023, 22: 2589−2599.

[18] DANG Cong, WANG Jing-feng, WANG Jin-xing, YU Di, ZHENG Wen-xuan, WANG Zi-hong, FENG Le, XU Chang-bing, CHEN Xian-hua, PAN Fu-sheng. The effect of β' precipitates on mechanical properties and damping capacity in the Mg−Gd alloy [J]. Vacuum, 2023, 215: 112230.

[19] JIANG H J, LIU C Y, ZHANG B, XUE P, MA Z Y, LUO K, MA M Z, LIU R P. Simultaneously improving mechanical properties and damping capacity of Al−Mg−Si alloy through friction stir processing [J]. Materials Characterization, 2017, 131: 425−430.

[20] LI Zhen-zhen, YAN Hong-ge, CHEN Ji-hua, XIA Wei-jun, ZHU Hua-ming, SU Bin, LI Xin-yu, SONG Min. Enhancing damping capacity and mechanical properties of Al−Mg alloy by high strain rate hot rolling and subsequent cold rolling [J]. Journal of Alloys and Compounds, 2022, 908: 164677.

[21] SU Ning, DENG Qing-chen, WU Yu-juan, PENG Li-ming, YANG Kun, CHEN Qiang. Deformation-induced dissolution of long-period stacking ordered structures and its re-precipitation in a Mg−Gd−Zn−Mn alloy [J]. Materials Characterization, 2021, 171: 110756.

[22] ABE E, KAWAMURA Y, HAYASHI K, INOUE A. Long-period ordered structure in a high strength nanocrystalline Mg−1%Zn−2%Y alloy studied by atomic-resolution Z-contrast STEM [J]. Acta Materialia, 2002, 50: 3845−3857.

[23] MAO Ping-li, XIN Yan, HAN Ke, LIU Zheng, YANG Zhi-qing. Formation of long-period stacking-ordered (LPSO) structures and microhardness of as-cast Mg−4.5Zn−6Y alloy [J]. Materials Science and Engineering A, 2020, 777: 139019.

[24] SUZUKI M, KIMURA T, KOIKE J, MARUYAMA K. Strengthening effect of Zn in heat resistant Mg−Y−Zn solid solution alloys [J]. Scripta Materialia, 2003, 48: 997−1002.

[25] HIRTH J P, LOTHE J. Theory of dislocations [M]. New York: McGraw-Hill Book Company, 1968.

[26] HAGIHARA K, YOKOTANI N, UMAKOSHI Y. Plastic deformation behavior of $Mg_{12}YZn$ with 18R long-period stacking ordered structure [J]. Intermetallics, 2010, 18: 267−276.

[27] LU Ruo-peng, WANG Jing-feng, CHEN Yong-liang, QIN De-zhao, YANG Wen-xiang, WU Zhong-shan. Effects of heat treatment on the morphology of long-period stacking ordered phase, the corresponding damping capacities and mechanical properties of Mg−Zn−Y alloys [J]. Journal of Alloys and Compounds, 2015, 639: 541−546.

[28] SHAO X H, YANG Z Q, MA X L. Strengthening and toughening mechanisms in Mg−Zn−Y alloy with a long period stacking ordered structure [J]. Acta Materialia, 2010, 58: 4760−4771.

[29] HUANG K, LOGE R E. A review of dynamic recrystallization phenomena in metallic materials [J]. Materials & Design, 2016, 111: 548−574.

[30] KABIR A S H, SANJARI M, SU J, JUNG I H, YUE S. Effect of strain-induced precipitation on dynamic recrystallization in Mg−Al−Sn alloys [J]. Materials Science and Engineering A, 2014, 616: 252−259.

[31] ROBSON J D, HENRY D T, DAVIS B. Particle effects on recrystallization in magnesium-manganese alloys: Particle-stimulated nucleation [J]. Acta Materialia, 2009, 57: 2739−2747.

[32] LIU Wei, MA Yan-bin, ZHANG Yong-gang, FAN Xin-xing, XU Chun-xiang, ZHANG Jin-shan. Two dynamic recrystallization processes in a high-performance extruded $Mg_{94.5}Y_2Gd_1Zn_2Mn_{0.5}$ alloy [J]. Materials Science and Engineering A, 2017, 690: 132−136.

[33] LEGORS M, DEHM G, ARZT E, BALK T J. Observation of giant diffusivity along dislocation cores [J]. Science, 2008, 319: 1646−1649.

[34] ZHANG Cheng-cheng, WANG Cheng, ZHA Min, WANG Hui-yuan, YANG Zhi-zheng, JIANG Qi-chuan. Micro-structure and tensile properties of rolled Mg−4Al−2Sn−1Zn alloy with pre-rolling deformation [J]. Materials Science and Engineering A, 2018, 719: 132−139.

[35] UMANTSEV A, ODE M. Formation of long-period stacking fault structures in magnesium alloys [J]. Computational Materials Science, 2016, 124: 173−182.

[36] WANG Kui, WANG Jing-feng, HUANG Song, GAO Shi-qing, GUO Sheng-feng, LIU Shi-jie, CHEN Xian-hua, PAN Fu-sheng. Enhanced mechanical properties of Mg−Gd−Y−Zn−Mn alloy by tailoring the morphology of long period stacking ordered phase [J]. Materials Science and Engineering A, 2018, 733: 267−275.

[37] XU Chao, NAKATA T, QIAO Xiao-guang, ZHENG Ming-yi, WU Kun, KAMADO S. Effect of LPSO and SFs on microstructure evolution and mechanical properties of Mg−Gd−Y−Zn−Zr alloy [J]. Scientific Reports, 2017, 7: 40846.

[38] WANG Kui, WANG Jing-feng, DOU Xiao-xu, HUANG Yuan-ding, HORT N, GAVRAS S, LIU Shi-jie, CAI Yan-wu, WANG Jin-xing, PAN Fu-sheng. Microstructure and mechanical properties of large-scale Mg−Gd−Y−Zn−Mn alloys prepared through semi-continuous casting [J]. Journal of Materials Science & Technology, 2020, 52: 72−82.

[39] XU Dao-kui, HAN En-hou, XU Yong-bo. Effect of long-period stacking ordered phase on microstructure, mechanical property and corrosion resistance of Mg alloys: A review [J]. Progress in Natural Science: Materials International, 2016, 26: 117−128.
[40] ONORBE E, GARCES G, DOBES F, PEREZ P, ADEVA P. High-temperature mechanical behavior of extruded Mg−Y−Zn alloy containing LPSO phases [J]. Metallurgical and Materials Transactions A, 2013, 44: 2869−2883.
[41] HAGIHARA K, KINOSHITA A, SUGINO Y, YAMASAKI M, KAWAMURA Y, YASUDA H Y, UMAKOSHI Y. Effect of long-period stacking ordered phase on mechanical properties of $Mg_{97}Zn_1Y_2$ extruded alloy [J]. Acta Materialia, 2010, 58: 6282−6293.
[42] CHEN R, SANDLOBES S, ZENG Xiao-qin, LI De-jiang, KORTE-KERZEL S, RAABE D. Room temperature deformation of LPSO structures by non-basal slip [J]. Materials Science and Engineering A, 2017, 682: 354−358.
[43] WANG Dan, LIU Shu-juan, WU Rui-zhi, ZHANG Shun, WANG Yang, WU Hua-jie, ZHANG Jing-huai, HOU Le-gan. Synergistically improved damping, elastic modulus and mechanical properties of rolled Mg−8Li−4Y−2Er−2Zn−0.6Zr alloy with twins and long period stacking ordered phase [J]. Journal of Alloys and Compounds, 2021, 881: 160663.
[44] NIE Jian-feng. Precipitation and hardening in magnesium alloys [J]. Metallurgical and Materials Transactions A, 2012, 43: 3891−3939.
[45] ZHENG Jing-xu, CHEN Bin. Interactions between long-period stacking ordered phase and β' precipitate in Mg−Gd−Y−Zn−Zr alloy: Atomic-scale insights from HAADF-STEM [J]. Materials Letters, 2016, 176: 223−227.
[46] GRANATO A, LUCKE K. Theory of mechanical damping due to dislocations [J]. Journal of Applied Physics, 1956, 27: 583.
[47] GRANATO A, LUCKE K. Application of dislocation theory to internal friction phenomena at high frequencies [J]. Journal of Applied Physics, 1956, 27: 789.
[48] SCHWANEKE A E, NASH R W. Effect of preferred orientation on the damping capacity of magnesium alloys [J]. Metallurgical and Materials Transactions B, 1971, 2: 3453−3457.
[49] SUGIMOTO K, MATSUI K, OKAMOTO T, KISHITAKE K. Effect of crystal orientation on amplitude-dependent damping in magnesium [J]. Transactions of the Japan Institute of Metals, 1975, 16: 647−655.
[50] ZHOU Xiong-peng, YAN Hong-ge, CHEN Ji-hua, XIA Wei-jun, SU Bin, YU Lang, HUANG Wen-sen, SONG Min. Effects of low temperature aging precipitates on damping and mechanical properties of ZK60 magnesium alloy [J]. Journal of Alloys and Compounds, 2020, 819: 152961.
[51] XU Chi, ZHANG Jing-huai, LIU Shu-juan, JING Yong-bin, JIAO Yu-feng, XU Long-jiang, ZHANG Li, JIANG Feng-chun, ZHANG Mi-lin, WU Rui-zhi. Microstructure, mechanical and damping properties of Mg−Er−Gd−Zn alloy reinforced with stacking faults [J]. Materials & Design, 2015, 79: 53−59.
[52] MA Ya-jie, LIU Chu-ming, HUANG Ying-jie, JIANG Shu-nong, GAO Yong-hao, WAN Ying-chun, CHEN Zhi-yong. Effect of extrusion parameters on microstructure, mechanical properties and damping capacities of Mg−Y−Zn−Zr alloy [J]. Journal of Alloys and Compounds, 2023, 935: 168122.
[53] WANG Dan, MA Xiao-chun, WU Rui-zhi, WU Hua-jie, WANG Jia-hao, ZHANG Shun, ZHANG Jing-huai, HOU Le-gan. Effect of extrusion plus rolling on damping capacity and mechanical properties of Mg−Y−Er−Zn−Zr alloy [J]. Materials Science and Engineering A, 2022, 830: 142298.
[54] SU Chen, WANG Jing-feng, HU Hao, WEN You-lin, LIU Shi-jie, MA Kai. Enhanced strength and corrosion resistant of Mg−Gd−Y−Al alloys by LPSO phases with different Al content [J]. Journal of Alloys and Compounds, 2021, 885: 160557.

通过调节 LPSO 与 β'相制备高强度和高阻尼 Mg−Gd−Y−Zn−Zr−Nd 合金

党 聪，王敬丰，王金星，余 迪，郑文瑄，许长冰，王自红，冯 乐，陈先华，潘复生

重庆大学 材料科学与工程学院 国家镁合金材料工程研究中心，重庆 400044

摘 要：采用合适的热处理工艺调节 Mg−Gd−Y−Zn−Zr−Nd 合金中层状 LPSO 相和 β'相的析出，研究层状 LPSO 相与 β'相对合金力学与阻尼性能的影响。实验结果表明，层状 LPSO 相更有利于动态再结晶过程，导致再结晶程度增加、织构强度降低，合金具有良好的塑性和阻尼性能。经过时效处理后，β'析出相具有显著的时效强化效果，并增加可动界面数量，使合金强度和阻尼能力同时提高。通过调节层状 LPSO 相与 β'相，合金获得高的强度与高的阻尼性能：极限抗拉强度为 498 MPa，屈服强度为 371 MPa，在应变为 1×10^{-3} 时，阻尼容量为 0.02。

关键词：Mg−Gd−Y−Zn−Zr−Nd 合金；强度；阻尼性能；β'析出相；LPSO 相

(Edited by Bing YANG)